GPS-PWV jumps before intense rain events

Luiz F. Sapucci[1], Luiz A. T. Machado[1], Eniuce Menezes de Souza[2], Thamiris B. Campos[3]

[1]Centro de Previsão de Tempo e Estudos Climáticos, Instituto Nacional de Pesquisas Espaciais, Cachoeira Paulista, Postal Code: 12630-000, Brazil.
[2]Departamento de Estatística - Universidade Estadual de Maringá, Maringá, Postal Code: 87020-900, Brazil
[3]Programa de Pós-Graduação em Meteorologia, Instituto Nacional de Pesquisas Espaciais, São José dos Campos, Postal Code: 12227-010, Brazil

Correspondence to: Luiz Sapucci (luiz.sapucci@cptec.inpe.br)

Abstract. A rapid increase in atmospheric water vapor is a fundamental ingredient for many intense rainfall events. High-frequency precipitable water vapor (PWV) estimates (one minute) from a Global Positioning System meteorological site (GPS) are evaluated here for intense rainfall events during the CHUVA Vale field campaign in Brazil (November-December 2011), in which precipitation events of differing intensities and spatial dimensions, as observed by an X-band radar, have been explored. A sharp increase in the GPS-PWV prior to the more intense events has been found and termed GPS-PWV "jumps". These jumps are associated with water vapor convergence and the continued formation of cloud condensate and precipitation particles. The correlation and lags between the high temporal resolution GPS-PWV time series and rainfall events are evaluated. A wavelet cross-correlation analysis shows that there are important spikes in the PWV that precede the more intensity/extension rainfall events on scales related to time periods from about 30 to 60 minutes. The GPS-PWV time-derivative histogram for the period of 60 minutes before the rainfall event reveals different distributions for higher intensity and extension events. This feature could indicate the occurrence of severe precipitation and consequently has the potential for application in nowcasting activities.

Comentário [s1]: Reviser1E3

Comentário [s2]: Reviser1E17

1 Introduction

The application of the Global Positioning System (GPS) tropospheric-induced signal delay to estimate the precipitable water vapor (hereafter, GPS-PWV) is a good example of an indirect solution for quantifying atmospheric humidity. The magnitude of this delay is related to the integral of the refractivity index of the air as a function of temperature, pressure and water vapor (Bevis et al. 1992) on the optical path followed by the GNSS signal. The wet component of this delay provides the precipitable water vapor (PWV) (Bevis et al. 1994), with an error of approximately 5% under all weather conditions (Wolfe and Gutman 2000) relative to other measurement techniques (Sapucci et al. 2007) and in near real time (Rocken et al. 1994). The methodology employed in GPS data processing has been improvement continually to minimize the uncertainty and the PWV estimate has been determined with an accuracy better than 2 mm (Moore et al. 2015; Shangguan et al. 2015) Although the vertical humidity structure is not captured in GPS-PWV estimates, the great advantage of GPS-PWV (in addition to its

all-weather capacity) is its high temporal resolution (minutes) (Zumberge et al. 1997). An important application of the GPS-PWV estimate is its assimilation into the Numerical Weather Prediction process, which has a positive impact on short-range forecasts of humidity fields and, consequently, better precipitation forecasts for heavy rainfall events (Cucurull et al. 2004; Bennitt and Jupp 2012). Other applications become viable in dense networks and transects. GPS-PWV has been useful for: studying the diurnal cycle of convective instability in Japan (Sato and Kimura 2005); investigating water vapor variability during a mistral/sea breeze event in southeastern France exploring GPS-PWV tomography (Bastin et al. 2005); studying water vapor diurnal cycle over African continent (Bock et al. 2008); evaluation of the GPS-PWV values before precipitation (Kursinski et al. 2008); tracking water vapor advection over Amazonian (Adams et al. 2011); GPS-PWV tomography have been used to investigate the water vapor distribution related to convective rainfall events and better understanding and quantification of the hydrological cycle in southeastern France (Brenot et al. 2014); it has been used to propagate convective events and determining topographic effects on the evolution of convection (Adams et al. 2015); studies of convective mesoscale events during the North American Monsoon (Serra et al. 2016) and nowcasting thunderstorm activities, as foreseen by Jerrett and Nash (2001). Guerova et al. (2016) showed development and test of new multi GNSS (Global Navigation Satellite System) products to forecasting of severe weather and emphasized the fact that for short-term, high-resolution forecasting or nowcasting models require more detailed humidity observation, e. g. GPS-PWV estimates.

The relationship between the occurrence of intense rainfall and high concentrations of atmospheric water vapor is well known and has been explored in nowcasting applications. Muller et al. (2009) described a model for the relationship between the PWV and convective precipitation event in the tropics. PWV data from a microwave radiometer (MWR) with high temporal resolution have been used to analyse and better understand the temporal relations of column water vapor and tropical precipitation (Holloway and Neelin, 2010). Chan (2009) evaluated the performance of a ground-based microwave radiometer in intense convective weather and reported an increasing degree of instability of the troposphere before the occurrence of heavy rain. In addition, he compared PWV from GPS and radiometer, the result showed that radiometer exhibited rather rapid fluctuations during intense precipitation, which are not observed in the GPS-PWV data. Madhulatha et al. (2013) reported a sharp increase in the PWV values approximately 2–4 hours prior to the occurrence of thunderstorms and developed a nowcasting technique using PWV values and 7 other thermodynamic indices from microwave radiometer observations. The relationship between deep convective activity and occurrence of intense rainfall and the temporal evolution of GPS-PWV has been studied for well over a decade. Mazany et al. (2002) developed a lightning prediction index for Florida based on the GPS-PWV magnitude and its temporal evolution. This index is a binary logistic regression model based PWV-GPS and other two variable predictors. The plot of the GPS lightning index time series showed a pattern several hours prior to a lightning, which was tested as forecasting tool of this events. Nowcasting employing GPS-PWV was reported by de Haan et al. (2004), who demonstrated its viability in improving thunderstorm and heavy precipitation forecasts during a cold front passage. De Haan (2006) developed a method for inferring the atmospheric stability from a nonisotropic GPS path-delay signal (slant delay). Book et al. (2008) carried out studies of the West African Monsoon using

Comentário [s3]: Reviser1E1

Comentário [s4]: Reviser1E2

ground-based GPS receivers and demonstrated the correlation between PWV and precipitation in seasonal and intraseasonal timescales. More recently, in the tropics, Adams et al. (2013) utilized 3.5 years of Amazon GPS-PWV to derive a water vapor convergence time scale associated with the shallow-to-deep convective transition. Given this one-hour lead time, near real-time GPS-PWV could, in principle, be employed to improve the nowcasting of these events. This study shown the PWV increase prior to heavy deep convective precipitation principally results from water vapor convergence, given that the surface evaporation is small in the cloudy, showery conditions preceding the event.

The motivation of the present study is to evaluate the large and rapid increases in the PWV characteristics prior to the onset of deep convective rainfall events observed during the CHUVA (Cloud processes of tHe main precipitation systems in Brazil: a contribUtion to cloud resolVing modeling and to the GPM (GlobAl Precipitation Measurement)) Vale experiment in Brazil in 2011 (Machado et al. 2014) using PWV estimates with high temporal resolution (one minute) from a GPS meteorological site. Adams et al. (2013) showed that prior to deep convective events in the central Amazon, a 4-hour "ramp up" in the time derivative of GPS-PWV is observed, reaching a maximum approximately one hour before heavy precipitation. This sharp increase in the GPS-PWV values before the occurrence of more intense rainfall events is hereafter termed the GPS-PWV jump. The GPS-PWV time series was evaluated using wavelet analysis in a study of correlation and lags with rainfall events to form a conceptual model with predictive capacity, which can be useful in nowcasting tool for strong precipitation events.

In section 2, we present the data collected during the CHUVA Vale experiment in Brazil and describe the GPS data processing technique for obtaining PWV values. An X-band radar was utilized to quantify the spatial-temporal distribution of the precipitation events. In section 3, the GPS-PWV jumps are defined and characterized. Section 4 presents the high temporal resolution GPS-PWV time series analysis, including wavelet analysis and time lag correlations between the precipitation and GPS-PWV time series, as well as the evaluation of GPS-PWV derivatives before precipitation events of different extensions. Finally, Section 5 presents the conclusions.

2 Data collection design and processing method

The data employed in this study were collected during the CHUVA Vale campaign, one of the field campaigns of the CHUVA project (Machado et al. 2014). The CHUVA project was designed to investigate cloud microphysical and precipitation processes through six intensive field campaigns covering various precipitation regimes in Brazil. The CHUVA Vale campaign was carried out in São José dos Campos City in São Paulo State (23° 12' 30" S and 45° 57' 08" W) in an elevated valley between the Mantiqueira and Serra do Mar mountain ranges. Fig. 1 shows the geographic location of the CHUVA Vale campaign. This region is dominated by deep convection with typical rainfall systems that are forced by sea breeze-mountain convergence zones as well as squall lines associated with cold front penetration (Machado et al. 2014).

Comentário [s5]: Reviser1E15

Comentário [s6]: Reviser1E3

Comentário [s7]: Reviser1E4

Comentário [s8]: Reviser1E4

2.1 Data from the CHUVA Vale experiment

The CHUVA Vale experiment consisted of an intensive observation period from November 3rd to December 28th of 2011. The instruments used in this study were a dual-frequency GPS receiver for scientific applications, a disdrometer and a mobile X-band dual polarization radar (XPol). The TRIMBLE brand GPS receiver, model NETR8 with Dorne-Margolin Choke Ring antenna, utilized in this study was installed 11 km from the XPol radar at the site denominated the Institute of Advanced Studies from the Department of Aerospace Science and Technology (IEAV) site. Any sky obstructions around the GPS receiver were avoided to minimize the multi-path effect in GPS signal propagation. See Fig. 1 for more details about the sites, at which the instruments were placed.

The GPS satellite signals were sampled at one-second frequencies, whereas the collocated meteorological sensor captured the pressure and temperature at one-minute frequencies. A Joss-Waldvogel brand acoustic impact disdrometer (Joss and Waldvogel 1967), model RD 80, was installed a few meters from the GPS receiver. The XPol radar scan strategy collected one volume scan every 6 minutes at 13 elevations, from 1° to 25°, with 1° and 150 m angular and radial resolutions, respectively. Due to a technical problem the radar was turn off in the period since 12:36 UTC of 14th November until 19:41 UTC of 15th November of 2011. The radar data were pre-processed using the attenuation correction of the reflectivity, employing the algorithm for ground-based polarimetric radars (ZPHI algorithm) proposed by Testud et al. (2000). For a detailed description of the radar and disdrometer pre-processing, see Calheiros and Machado (2014).

Comentário [s9]: Reviser1E5

2.2 High temporal resolution GPS-PWV time series

The zenith total delay (ZTD) was obtained by processing the GPS data using GOA-II [(Gipsy, GPS Inferred Positioning System) (OASIS, Orbit Analysis and Simulation Software II) Gregorius 1996] software by applying the precise point positioning method in post-processing mode with the precise ephemerides of the GPS constellation provided by the NASA Jet Propulsion Laboratory. Sampling rate of the used GPS satellites ephemeris is 15 minutes for orbits and 5 minutes for GPS satellite crock.

To ensure the quality of the PWV time series with high temporal resolution required in this study, in the data-processing strategy adopted the known uncertainty sources were taken into consideration applying the recommended models and adjustment of parameter exploring available stochastic models. The latest version of the GOA-II software (version 6.3) was used, which estimates parameter with high temporal resolution exploring the sophisticated orbit integrator package to estimate GPS satellite position in each epoch. The ocean tide model FES 2004 (Lyard et al. 2006), recommended by the International Earth Rotation and Reference Systems Service (IERS Conventions 2010) was applied in this processing. Method of antenna absolute calibration (Schmid et al. 2007) was applied by GOA-II to ensure the correct phase center variation of the satellites and receiver antennas using parameters provide by IGS web site (Montenbruck et al. 2015). The data processing with GOA-II software to obtain ZTD estimates was done selecting the Global Mapping Function (Boehm et al. 2006) and the sampling rate of the ZTD estimates of 60 seconds. The others possible parameters that can be selected were

used the configuration basic suggested by JPL. As the configuration items associated with ZTD estimates and respective values used can impact in the variability of the ZTD in high temporal resolution (basic information used in this study), they are listed in Table 1 in order to highlight them.

The zenith wet delay was obtained from the ZTD after removing the zenith hydrostatic delay obtained through the application of a representative tropospheric temperature model and a surface pressure measurement (Davis et al. 1985). The zenith wet delay was converted into the PWV using the relationship suggested by Bevis et al. (1992). The mean tropospheric temperatures (Tm) with sampling rate of 1 minute were obtained from the temperature and pressure measured at the GPS antenna by applying the regional model suggested by Sapucci (2014), which is the most suitable for this region. The sampling rate of the GPS-PWV values was 1 minute. The GPS-PWV time series suffered some short failures due to interruptions in data collection, problems with the incomplete satellite ephemerides file from JPL website and unavailable pressure measurements. These time series interruptions occurred in 3,183 epochs (3.1% of the total period), and the missing values were filled by a cubic spline interpolation method specific for application of wavelet analysis, which requires complete time-series without failures. These interpolation were concentrated in two specific days [Day of Year (hereafter called DoY) 331 and 348] and these periods were removed of the data analysis.

2.3 Precipitation time series from disdrometer and XPol radar data

The reason for choosing one disdrometer to quantify the precipitation is that this instrument is able to provide an instantaneous measurement of the rainfall intensity (mm h^{-1}) at the same GPS-PWV sampling rate; however, this information is only representative of a very small spatial scale (sampling area of the 50 cm^2). Notably, the XPol radar data are able to generate information with a different and more representative spatial resolution around the GPS receiver.

The precipitation rates were obtained from the Joss disdrometer data by applying the methodology suggested by Kinnell (1976), in which the precipitation intensity of each minute is inferred from the size and concentration of the rain drops observed during this time period. The precipitation data from the XPol radar observation were obtained by applying the Dual Polarization Surface Rainfall Intensity algorithm, which calculates the rainfall rate (R) from the reflectivity (Z) and specific differential phase data obtained in multiple-elevation polar volumes. In this method, polarimetric measurements are used to calculate R by applying a combined Z R relationship (Gematronik 2007). The final product of this process is a gridded map (100-km radius around the XPol) with a horizontal resolution of 200 m, in which each of the grid point values of the rainfall intensity (mm h^{-1}) at a sampling rate of 6 minutes is available.

The area around the GPS receiver taken into consideration to calculate the time series of the precipitation fractional observed by radar was a quarter with GPS antenna in the center. In the practical, the position of the GPS antenna was determined in the gridded precipitation points from Radar data and the same number of points in all direction (North, South, East and West) were used to composite this area. Fig. 1 shows the details of the composition of this area using points from the XPol gridded map. The dimensions of the precipitation area that influences the GPS-PWV is a key factor in the

Comentário [s10]: Reviser1E6

development of this study because its choice is associated with the lead time of the GPS-PWV information indicating strong precipitation. A reduced precipitation area around the GPS antenna (e.g., values measured via a rain gauge) is not sufficient to represent the rain associated with a significant variation in the GPS-PWV time series. However, larger areas permit distant precipitation (which is not directly associated with the GPS-PWV measurement) to be taken into account. Different areas were tested, such as 110x110, 60x60 and 22x22. , and an area of 22x22 [longitudinal per latitudinal direction grid point values of rainfall intensity (mm h^{-1})] was found to be more adequate to associate the observed area by GPS with precipitation observed by Radar and to exploring the correlation between the thunderstorms occurrence and GPS-PWV variations. The resultant area is 4.4 km per 4.4 km (~20 km^2) around the GPS antenna. Although this area does not exactly match the cone of the GPS observation, it was chosen because it most highly correlates with the precipitation measurements taken by radar in this square area of ~20 km^2 which the GPS antenna is located in the center. The rainfall area employed in this study is only a reference for the description of the GPS-PWV jump. Notably, the area employed has the highest correlation with GPS-PWV, but it is expected to vary as a function of the region and satellite configuration. Fig. 1 shows the configuration of the XPol radar, GPS antenna and disdrometer in the CHUVA Vale experiment and highlights the mentioned area of 4.4 km per 4.4 km around the GPS antenna. The precipitation field observed by XPol on December 14th (DoY 348) is presented in Fig. 1 to illustrate the points from the XPol gridded map used to represent the precipitation area around the GPS antenna taken into account in this study. This event was chosen because it was the most intense, with 70% of the area around the GPS antenna recording precipitation above 50 mm h^{-1}.

Comentário [s11]: Reviser1E7

As the focus here is to study the GPS-PWV behavior during intense rainfall, the statistical measurements calculated from the radar data were in the 95th percentile of the intensity of the precipitation observed in the area of 4.4 km per 4.4 km around the GPS antenna. Additionally, to evaluate rainfall events of different intensities, the rain fraction was computed as the fraction of area of 4.4 km per 4.4 km around the GPS antenna with precipitation rates above some chosen threshold. The first approach emphasizes the more intense localized precipitation events, and the second simultaneously quantifies the intensity and extension of each event. The chosen thresholds were computed to create time series of the following rainfall event intensities: moderate to heavy (20 mm h^{-1}), heavy to intense (35 mm h^{-1}) and intense to torrential (50 mm h^{-1}). The disdrometer was used in this study only for a reference and for comparison with the radar rainfall estimations. Fig. 2 presents time series of the GPS-PWV (Fig. 2a), the precipitation from the disdrometer data (Fig. 2b) and, from the XPol radar, the 95th percentile of the precipitation intensity (Fig. 2c) and the rain fractions for different thresholds (Fig. 2d). The period studied here is from November 9th (DoY 313) to December 28th (DoY 362) of 2011, during which the GPS receiver, XPol radar and disdrometer were simultaneously collecting data. The figure show that the disdrometer time series is consistent with the 95th percentile time series, although differences are expected due to the different areas covered by each instrument and besides total precipitation from disdrometer is always larger than the one measured by radar and raingauge, due to problems with the large droplet concentration (Giangrande et al. 2016).

Comentário [s12]: Reviser1E8

Comentário [s13]: Reviser1E17

3 Behavior of PWV time series before precipitation events: the GPS-PWV jumps

The high temporal resolution obtained with the GPS-PWV enables the evaluation of high frequency variations and their relationship with intense precipitation events. The GPS-PWV time series shows a well-defined sharp increase before the occurrence of precipitation, as reported by Kursinski et al. (2008) as a rapid rise in PWV preceding the rain events. Shi et al. (2015) using GPS -PWV to monitoring the water vapor variation shown that ascending and descending patterns of GPS-PWV can be identified before and after each rainfall event. There are strong oscillations, generating a significant increase in the total water vapor content until a maximum is reached. Subsequently, a strong GPS-PWV reduction is observed, and after a short interval, the precipitation also reaches a maximum peak. Here, this sharp increase is called GPS-PWV jump. Fig. 3 shows a typical case exemplifying the PWV behavior before precipitation occurs on DoY 341; this was one of the strongest events registered during the CHUVA Vale experiment. Before the severe precipitation begins, the GPS-PWV follows several pulses, increasing the value and forming the PWV jump, until it reaches a peak of maximum value. After the GPS-PWV crest, a decreasing period is observed some minutes before severe precipitation. Fig. 3 clearly shows this configuration of a crest in the GPS-PWV time series around precipitation (composed of several pulses) and its subsequent decrease immediately before the beginning of stronger precipitation.

Comentário [s14]: Reviser1E17

This GPS-PWV behavior before precipitation occurs not only for more intense events but also for lower rainfall rates. Fig. 4 shows other GPS-PWV jumps observed before rain events with different intensity/extension occurred on: DoY 315 (41% of precipitation fraction above 35 mm h^{-1}), DoY 332 (5%) and DoY 358 (only 1% of precipitation fraction above 35 mm h^{-1}). This figure shows the intensity of these sharp increases in GPS-PWV are larger before more extensive precipitation. Table 2 presents all precipitation events in which the rainfall above 20 mm h^{-1} was observed by XPol radar in the area of 4.4 km per 4.4km around GPS antenna. This table presents the DoY and time of maximal radar precipitation of the each event and the respective fraction rain above 20 mm h^{-1}, 35 mm h^{-1} and 50 mm h^{-1}. In order to obtain an overview of the hardiness of the GPS-PWV jumps feature before precipitation, Fig. 5 show the composite mean of GPS-PWV time series from 60 minutes before to 60 minutes after maximum observed precipitation (fraction rain above 35 mm h^{-1}) for 18 events listed by Table 2. The composite presented in Fig. 5 is normalized by maximum GPS-PWV values before precipitation. The composite mean shows that the GPS-PWV jump is strongly remarkable before the maximum precipitation, which the maximum of the composite mean is observed in 30 minutes and lower dispersion in 25 minutes before the maximum precipitation. The time lag between the maximum GPS-PWV and the time of the maximum rainfall is presented in a sub plot in Fig.5. It is important highlight that the there are many precipitation events of lower intensity and extension in which the GPS-PWV jumps are not observe. In these cases, the maximum GPS-PWV is observed in the maximum precipitation, consequently the time lag is zero (37% of the cases evaluated). In this histogram, it is clear there is a range of lag time between the GPS-PWV and precipitation maximums, the precipitation area and the temporal resolution of GPS-PWV here employed have an impact on this lag time. For instance, Adams et al. (2013) using rain gauge and PWV with sampling rate of 30 minutes over Amazonian region found out lag zero, however, in this study we shows that the GPS-PWV signal can represent a precipitation area and

not only a punctual measurement over the GPS antenna. An analysis of the time lag correlation is necessary to define this interval between the maximal GPS-PWV and precipitation, which is carried out in the next section.

The physical explanation for this behavior could be explained by different physical processes. First, the water vapor may increase through low-level moisture convergence. The variation of the moisture convergence generates a sequence of pulses of positive increases in the PWV value. The sequence of pulses of positive increases in the PWV could be a result of several physical processes. Some of the physical process that can explain these pulses could be low-level water vapor convergence forced by gravity wave (Raymond 1987) or simply unstable surface parcels accelerating upwards. After the increase of GPS-PWV at the crest of the jump, rainfall starts and PWV starts to decrease. The lag time between the crest and the maximum precipitation can vary from one region to another, from one rainfall cell to another because it depends on the cloud condensation nuclei and the precipitation efficiency, normally a function of the wind shear. In this study using precipitation measures based on area about the GPS antenna, we found a time lag between these maximum. Addams et al. (2013) considered that the conversion of water vapor to liquid water and precipitation are of second order during the process of PWV increasing. It is probably true during the phase of cloud formation, however, when the precipitation starts, water vapor decreases due to the formation of liquid water. The conversion of the water vapor to liquid water changes the dielectric medium, where the refractivity is induced by the displacement of charge (Solheim et al. 1999). While the refractivity from water vapor is due to the polar nature of the water molecule, the GPS phase delay induced by liquid water (hydrometeor) is proportional to the electric permittivity of the formed dielectric medium and, consequently, much lower than the delay generated by water vapor. Another important physical mechanism is the storm downdraft that is dryer and colder that the ascending moisture air and this downdraft can also contributes to the decrease in PWV. In addition, PWV decreases after precipitation starts can be simply associated to the final process of surface convergence as function of the rainfall and downdrafts on the surface, or by the advection process forced by the shear and storm movement. Given the limitations of the observations, our interpretation of the physical mechanisms responsible for the jumps remains speculative. To understand what the physical mechanisms responsible for the pulses and GPS-PWV jumps, a specific field campaigns design are needed.

4 High temporal resolution GPS-PWV time series analysis

The high temporal resolution GPS-PWV time series and precipitation in different intensity and extension are evaluated and the PWV-GPS jumps are characterized. The wavelet analysis are explored to evaluating which the timescale of the GPS PWV oscillations are associated with a more intense rainfall occurrence and time lag correlation analysis are used to determine the lag between the rainfall intensity and the GPS-PWV time series. Additionally, PWV-GPS derivative analysis is explored and its potential for nowcasting application is discussed.

4.1 Wavelet analysis

Wavelet analysis was used to perform a detailed analysis of the GPS-PWV time series and to evaluate the variability within different time scales (denoted here as intra-relation), as well as to assess the relationship between the GPS-PWV time series and the precipitation time series (denoted here as interrelation wavelet analysis). This methodology enables simultaneous decomposition of the PWV time series as a function of time and frequency (Daubechies 1992). Consequently, accessing to the information regarding the signal amplitude/frequency and its variation as a function of time becomes possible.

To perform the intra-relation analysis evaluation of how spectral characteristics change over scales (s) and time (t), but with highly redundant information, the continuous wavelet analysis (Torrence and Compo 1998) was used to estimate the wavelet power spectrum. Thus, a decomposition of the GPS-PWV data into time-variability space allows an evaluation of the main frequencies composing the GPS-PWV time series during intense rainfall events. With continuous analysis, some hidden features of the time series can be identified, e.g., in which scale are the most representative behaviors of the time series. Continuous analysis is often easier to interpret because its redundancy tends to reinforce the traits and makes all information more visible. However, for some specific choices of values for time and frequency, it is possible to apply a discrete wavelet transform, which does not lose important information and has advantages of implementation and computational effort. This is the case of the non-decimated discrete wavelet transform (NDWT), also called Maximal Overlap Discrete Wavelet Transform, which can be seen as a compromise between the discrete wavelet transform (DWT) and CWT because of its redundancy, but not as redundant as CWT. The NDWT can be computed similarly to the ordinary DWT but without subsampling (decimation), ensuring the translational invariance, which is ideal for analysing time series, especially interrelations between different time series. A time-variant transform disrupts the lag-resolution in a cross-correlation analysis. Furthermore, estimators calculated using the NDWT are considered more preferable because they are asymptotically more efficient than the estimator based on the DWT (Percival and Walden 2000). As the bivariate relationship between two time series is essential for this research, a wavelet cross-correlation (WCC) constructed from NDWT (Whitcher et al. 2000) is ideal for analysing different scale structures and the interrelations of the dynamic behaviour of two time series, as well as the lead-lag relationships. Some lead-lag relations that could not be distinguished in the usual cross-correlation can be investigated in the WCC, which decomposes the cross-correlation on a scale-by-scale basis. Thus, a specific scale may be associated with water vapor convergence before precipitation occurrence, also providing a lead time for nowcasting, a specific time scale for calculations and additional information to understand the physical mechanisms associated with intense rainfall events in this region.

Comentário [s15]: Reviser1E9

Considering the large quantity of available discrete mother wavelets, some of the most used in the literature were evaluated: Daubechies with 4, 6, 8, and 16 coefficients, denoted by D4, D6, D8, D16, and Daubechies Least Asymetric with 8, 16, and 20 coefficients, denoted by LA8, LA16, and LA20, respectively. To verify the statistically significance of the estimated wavelet correlations, the 95% confidence interval was estimated considering a Gaussian Distribution after applying the Fisher`s Z Transformation (Whitcher et al. 2000).

Comentário [s16]: Reviser1E14

Because of implementation aspects considered in this study, the two time series were restricted to a power of two length, with 65,536 (2^{16}) observations, excluding one day at the beginning and another at the end of the GPS-PWV series. The time span corresponds to 45 days, 12 hours and 16 minutes, beginning on DoY 314 (00 UTC 10 November) and finishing on DoY 359 (1216 UTC 27 December). The same time series length was used for both intra- and interrelation analyses. Because each wavelet scale j in the interrelation analysis corresponds to a frequency band from 2^j to 2^{j+1}, its inversion allows the interpretation in terms of a period of time also in a dyadic interval. Thus, WCC enables the identification of the most important scale of the PWV oscillation during precipitation events. Furthermore, the WCC of GPS-PWV and precipitation time series also allows evaluating the lead-lag correlation that may exist between these time series for the different time periods.

4.1.1 Wavelet power spectrum analysis

For an intra-relation analysis, the wavelet power spectrum of GPS-PWV and 95th percentile of the precipitation intensity time series are presented in Fig. 6. To emphasize the highest-frequency oscillations, the power spectrum in Fig. 6 shows the scales that represent the period below 512 minutes (~8.5 h). The PWV diurnal cycle presents strong power along all time series, and consequently, it was not taken into consideration in this analysis. The range of power spectrum associated with color scale used in Fig. 6 is for scales related to time periods larger than 16 minutes.

The PWV series with a one-minute temporal resolution presents oscillations of high frequency; however, the frequency of occurrence of rainfall events is very low. For this reason, it is necessary to take into consideration a long time period (with several precipitation events) and a short time step, e.g., the one-minute interval used in this study. Consequently, in a general analysis of the PWV wavelet power spectrum, it is difficult to clearly discern which power is associated with each time step. However, a more specific analysis of the wavelet power spectrum during precipitation events indicates that there are, as expected in function of described GPS-PWV jump, strong changes in the power between different scales; cases with an increase in the power of the oscillation from low to high frequency are observed. This result indicates that PWV oscillations on scales related to time periods smaller than 128 minutes occur more frequently during precipitation events than in periods without rain. Fig. 7 presents the same wavelet power spectrum presented in Fig. 6 but with an enlargement applied for precipitation events observed during the period from DoY 340 to DoY 343. The analysis of the power spectrum in these cases makes the result discussed for Fig. 6 more understandable. For clarity, a vertical line was drawn for each precipitation maximum. Fig. 7 shows that the power of the PWV oscillations between 128 and 32 minutes is stronger during more intense precipitation events (for example, the events that occurred on DoY 341 at 1836 UTC and DoY 342 at 1636 UTC) than during light rainfall events (events observed during DoY 343) and periods without rain (DoY 340). It is interesting to observe that GPS-PWV presents a jump at the end of the DoY 357 with a strong signal in the wavelet power spectrum, but XPol radar did not detect any precipitation. The wavelet power spectrum (Fig. 6) also shows the impact of the GPS failures

Comentário [s17]: Reviser 1E10

Comentário [s18]: Reviser1E11

Comentário [s19]: Reviser1E12

Comentário [s20]: Reviser1E11

that occurred during DoY 331 and 348, which are unfortunately very close to the other intense precipitation events that occurred on DoY 332 and 348. For this reason, these cases are not spotlighted in the wavelet analysis.

4.1.2 Wavelet cross-correlation analysis

Before presenting the inter-relation results, one might question about the robustness of the method regarding the choice of mother wavelets. We estimated the wavelet correlations using Daubechies and Least Asymetric wavelets with different filter lengths (coefficient number) as presented in Section 4.1. The results were quite similar independently of the mother wavelet, but the correlations were maximized when the mother wavelet has a larger filter or more coefficients (D16, LA16, and LA20). Thus, all estimated wavelet correlations were presented using the LA20 mother wavelet. Fig. 8 shows the wavelet correlation and its 95% confidence interval between the GPS-PWV and the 95th percentile of the precipitation intensity as a function of the wavelet scale, represented by the respective time periods, considering the lag zero. In this analysis, the precipitation data from XPol radar, originally with sampling rate of 6 minutes, were linearly interpolated to one-minute rate. The results show that the wavelet correlation between the PWV and precipitation intensity is stronger for the scale related to the period between 32 and 64 minutes, indicating the scale on which the most important GPS-PWV oscillations associated with precipitation events occur. After this scale, the correlation decreases, followed by another increase due to the influence of the diurnal cycle. Although the correlations are not very high, 95% confidence interval showed that these results are statistically significant.

To evaluate the results presented in Fig. 8 for different intensity and extension of precipitation events, Fig. 9 shows the wavelet correlation for lag zero between GPS-PWV and precipitation fractions as a function of the period bands for different rain fraction intensities (>20 mm h^{-1}, Fig. 9a; >35 mm h^{-1}, Fig. 9b; and >50 mm h^{-1}, Fig. 9c). The 95% percentiles give an information about the maximum rain rate (which can be only one point) on the area of 4.4 km per 4.4 km around the GPS antenna. The rain fraction gives an information about the fraction of these studied area covered by rain rate above of these thresholds. There are some events where the rain intensity can be high and the fraction small, for instance, the cases of isolate clouds. Therefore, the area fraction presents a more close representation of rainfall events related to low level convergence because it gives information about the amount of liquid water in the area. The peak of the wavelet correlation observed in the time period from 32 to 64 minutes is significant for the three rain thresholds. The plots of Fig. 9 also show when only heavy to torrential precipitation events are taken into consideration (hereafter called intense rain events), stronger wavelet correlation is observed.

To perform the lead-lag analysis, the WCC is showed in Fig 10 between GPS-PWV and rain fraction for different intensities (>20 mm h^{-1}, Fig. 10a; >35 mm h^{-1}, Fig. 10b; and >50 mm h^{-1}, Fig. 10c). Although the precipitation and GPS-PWV time series present very distinct behaviors, the WCC permitted the identification of the correlation in lead-lag of about 30 minutes mainly for scales related to time periods from 32 to 64 minutes, indicating which GPS-PWV oscillations are important for predicting precipitation events. This results show also that considering the rain fraction for stronger intensities (>50 mm h^{-1}), some statistically significant correlations in lead-lag of about 30 minutes also appear stronger from period bands of 4- 16

Comentário [s21]: Reviser1E13

Comentário [s22]: Reviser1E14

Comentário [s23]: Reviser1E11

Comentário [s24]: Reviser1E1

and 16-32 minutes. This result indicates that the GPS-PWV carries some information, mainly, on the scale related to the period from 32 to 64 minutes. That signals the occurrence of precipitation events of large intensity and extension, which suggests that the GPS-PWV jumps are, for these storms evaluated, concentrated in this scale emphasizing its potential in a nowcasting application. It is also important to highlight that the correlation is larger on this scale than on adjacent scales. Furthermore, these results indicate that, although GPS-PWV jump before precipitation occurs not only for more intense events, the intensity of these oscillations associated to jumps is greater before the most intense and extensive ones. However, this feature should be considered as specific to each region because the time scale between the humidity convergence and rainfall may depend on many physical processes and environmental conditions (e.g., gravity wave-induced convergence, wind shear or thermodynamic instability).

Comentário [s25]: Reviser1E15

4.2 Time lag correlation analysis

The relationship between the rainfall intensity (or rain fraction) and the GPS-PWV is different for each event; however, the GPS-PWV peak is a well-delineated pattern. The time interval between the moment of the PWV crest and the maximal precipitation can vary among cases. The WCC shows on which scale the correlation between GPS-PWV and precipitation time series is higher, as well as the lead-lag interrelation between them. However, evaluating the lag correlation for positive and negative correlations is also important for further developing nowcasting tools. Fig. 11 shows histograms of the lag correlations (the time lags for the maximum and minimum correlations) between GPS-PWV and rain fraction for all events in which the rainfall rate observed around the GPS antenna was above 20 mm h^{-1}. The 18 events listed in Table 2 were evaluated, in which different rain fractions were observed using XPol radar. The histogram was constructed based on the correlation time lags found for the positive correlation (maximum) and negative correlation (minimum). The search time lag interval for the positive (negative) correlation was restricted for a period before (after) the precipitation because there are some subsequent rain events very nearby that could distort the results.

The type of correlation used in this study was Spearman's ρ (Best and Roberts 1975) because the GPS-PWV does not have a normal distribution. Additionally, the statistical significance of each correlation was evaluated by rejecting the hypothesis of a null correlation when the p-value was smaller than a 5% significance level.

The histograms presented in Fig. 11 indicate that the GPS-PWV crests are more frequent in the time interval between 15 and 30 minutes before maximum precipitation occurs (39% of the cases evaluated), and 85% of the positive correlations occurred between 15 and 60 minutes. After the rainfall events, when the GPS-PWV decreased, the time lag observed was between 15 and 60 minutes. In 50% of the cases, the minimum GPS-PWV occurred between 45 and 60 minutes. As already mentioned, several mechanisms can be responsible for the PWV decrease, and the specific physical process for each event can vary. This result corroborates the pattern observed in Fig. 3, which shows the GPS-PWV maximum before the precipitation event and its minimum after the maximum precipitation, which indicates a conceptual model that can be explored for nowcasting applications.

4.3 GPS-PWV derivative analysis: potential for nowcasting application

To evaluate the GPS-PWV derivative before precipitations of different intensities, taking into consideration the extension of the events, the area fraction with precipitation observed was used. Fig. 12 shows the distribution of the GPS-PWV time derivative for the period of 60 minutes before the maximum peak of precipitation for the 18 evaluated events for different terciles of rain fraction (>35 mm h^{-1}). The size of the time-window used here is based on wavelet correlation results, which given the clear indication that PWV-GPS oscillation for the scale related to this period are associated with stronger precipitation events. This precipitation threshold was employed in this analysis because it has been shown to be the lowest threshold (among the 3 that were tested) of rainfall intensity evaluated that presents a significant WCC between the GPS-PWV and precipitation in this time window. Table 2 shows the list of rainfall events in the terciles and the precipitation fraction observed using XPol radar during the maximum precipitation peak for each event. In Fig. 2d, each event can be visualized by observing the respective DoY. The same calculation was conducted for periods with rainfall events of intensities smaller than 20 mm h^{-1} including periods without observed precipitation, which is denominated in Fig. 12 as "other cases". The derivatives were calculated every minute using a Δt of 6 minutes. This interval time was selected because it is the sampling rate of the precipitation observed using XPol radar. The statistical metrics of the derivative for different terciles of the precipitation extension are shown in Table 3.

Fig. 12 clearly shows a strong change in the pattern of the derivative distribution as a function of the different precipitation extension terciles. In the period without significant rain, the derivative frequency distribution is similar to a Gaussian distribution with an average of zero and a standard deviation of 2.5 mm h^{-1}. However, the average of the derivative increases when the precipitation fraction increases, and the maximum peak changes to positive values for higher terciles. Notably, this effect is observed for the middle and upper terciles and nearly undetectable for the lower terciles. The lower terciles represent the events with observed precipitation in a reduced area, and the derivative histogram shows that in these cases, the differences are small between rain events smaller than 20 mm h^{-1} and periods without observed precipitation. This pattern impacts the average value of the derivative, which is +0.13 kg m^{-2} h^{-1} (±5.57 mm h^{-1}) for the upper tercile, -0.38 mm h^{-1} (±4.76 mm h^{-1}) for the middle tercile and -0.18 mm h^{-1} (±3.18 mm h^{-1}) for the lower tercile.

The negative derivatives (the majority of which occur after the peak maximum GPS-PWV) less than -9.5 mm h^{-1} are more frequent for events with a larger precipitation fraction, such as the upper and middle terciles (5.47% and 4.68%, respectively), than for the events contained in the lower tercile, in which these derivative values are not observed. One possible reason for this increase in the stronger negative derivative frequency before more extensive events (upper and middle terciles) is the conversion process from water vapor to liquid water.

The GPS-PWV derivative analysis showed that the majority of the positive derivative frequencies occur before the peak maximum GPS-PWV. The positive derivative above +9.5 mm h^{-1} increases more substantially before rainfall events in the upper tercile (7.81%) than for events in the middle (0.78%) and lower terciles, which are not observed. In other words, these derivatives are associated with PWV pulse and are important in the frequency distribution when the rainfall tercile increases

and are significant before the most precipitation-extensive events. Fig. 13 shows the time series of GPS-PWV derivative before precipitation events of the upper tercile, and emphasizes the occurrence of this stronger derivative (above +9.5 mm h^{-1}) observed at least three of the evaluated events. These stronger derivatives, associated to PWV pulses, occur with larger frequency in the period from 55 to 25 minutes before the maximum precipitation, which is GPS-PWV jump is observed and the pick of PWV maximum also occur.

Although the GPS-PWV pattern before precipitation described in the previous section is well defined, its use as an index for the occurrence of severe storms is not simple. Several studies have taken into account the intensity of rainfall events. Therefore the use of only a maximum threshold from a GPS-PWV derivative, as suggested by Iwabuchi et al. (2006) and Shi et al. (2015), is not sufficient to predict intense rainfall, several atmosphere processes are very complex and highly nonlinear. The intensity of the precipitation is highly correlated with the intensity of the PWV value, which is formed by a succession of pulses of positive increases in the PWV value. Therefore, the occurrence of more intense rain is signaled not only by the maximum derivative but also by the increase in the frequency distribution of the positive and negative derivatives before the occurrence of precipitation.

The result found by GPS-PWV derivative analysis suggests that an algorithm for intense precipitation forecasting using the GPS-PWV should consider the following points: (a) increases in GPS-PWV positive variations compared with negative ones in which the median values of the variation in the last 60 minutes reach positive values and (b) a simultaneous increase in the population of the GPS-PWV derivatives above +9.5 mm h^{-1}. The value of the stochastic constrains applied on temporal evolution of ZWD during the GPS data processing can make influence the PWV variability in high temporal resolution. The value used in this study was the default, but some tests with different constraint can be carried out to identify the impact of this parameter in the derivative analysis before intense precipitation.

The GPS-PWV values evaluated in this study are post-processed, and an additional study is required to determine whether these estimates in real time are able to capture the jumps before the precipitation reported. True real-time processing for PWV estimates in dense and regional GPS networks has been explored in other studies related to nowcasting applications (Iwabuchi et al. 2006). De Haan and Holleman (2009) reported the construction and validation of a real-time PWV map from a GPS network combined with data from weather radar, a lightning detection network, and surface wind observations. They tested a nowcasting algorithm for three thunderstorm case studies and concluded that the GPS-PWV in real time can be helpful for the nowcasting of severe thunderstorms. Shi et al. (2015) studied the PWV estimates in real time for rainfall monitoring and forecasting and shown that this estimate has quality comparable with post-processed product. A significantly reduction in the latency was obtained with GPS data processing proposed by Shi et al. (2015), which demonstrated promising perspective of the PWV-GPS data for rainfall forecasting.

5 Conclusions

This work evaluates the correlation between large and rapid increases in the GPS-PWV and the occurrence of rainfall events observed by radar during the CHUVA Vale experiment in Brazil. A detailed analysis of the GPS-PWV time series was carried out, and strong and sudden sharp increase composed predominantly by positive derivatives, before the precipitation events were identified and called as GPS-PWV jumps. In this process, a crest in the PWV series is remarkable before the precipitation events. Although this sharp increase can be observed for any precipitation event, it is preponderant before more intense and extensive precipitation events.

The wavelet analysis for the GPS-PWV time series was explored to characterize the strong changes in the power spectrum between different time scales during precipitation events generated by the occurrence of the GPS-PWV jumps. Additionally, the application of wavelet cross-correlation between the PWV and precipitation showed that important oscillations exist between these variables on the scale related to a time period from 32 to 64 minutes, which is stronger for events of large intensity and extension. These results corroborates with those reported by Adams et al. (2013), who showed that the strongest water vapor convergence is typically ~1 hour before heavy precipitation.

A time lag-correlation histogram shows that in 85% of the studied events, a crest in the PWV time series occurs between 15 and 60 minutes before the maximum precipitation. The GPS-PWV derivative histogram shows the distribution change for different precipitation extension terciles. The average values of the GPS-PWV derivatives present an increase in positive values as a function of the increase in the rainfall extension terciles. The results suggest that the derivative average values in the interval of 60 minutes before precipitation changes to positive values, and an increase in the frequency of the derivative above +9.5 mm h^{-1} can indicate the occurrence of severe precipitation. Consequently, a methodology based on the monitoring of the GPS-PWV derivative histogram presents potential for exploration in nowcasting applications, but additional studies will be necessary to define an appropriate algorithm and characterize the skill of this tool using the GPS-PWV estimates in real-time.

Comentário [s26]: Reviser1E11

Comentário [s27]: Reviser1E15

Competing interests: The authors declare that they have no conflict of interest.

Acknowledgments: The authors are grateful to David Adams and three AMT's reviewers for their many constructive comments, which helped us to improve the technical and scientific quality of this paper. Thanks are given to the CHUVA team who were involved directly or indirectly in the data collection by XPol radar, disdrometer and GPS receiver during the CHUVA-VALE experiment in São José dos Campos-S.P. Special thanks is given to Thiago Souza Biscaro. This study was supported by the Fundação de Amparo a Pesquisa do Estado de São Paulo (FAPESP), which directly supported this experiment [Grant Process 2009/15235-8 (CHUVA project)], and the Contractual Instrument of the Thematic Network of Geotectonic Studies CT-PETRO (PETROBRAS) and INPE (Grant: 600289299), which provided the GPS receiver used in this experiment. The raw data (Level 0) from the XPol radar, disdrometer and GPS receiver used in this study and the values

obtained by applying the methodology reported in section 2 (Level 2) are freely available through the Brazilian Institute for Space Research (ftp://pararaca.cptec.inpe.br/) after registration in the CHUVA-PROJECT portal (http://chuvaproject.cptec.inpe.br).

References

Adams, D. K., R. M. S. Fernandes, E. R. Kursinski, J. M. Maia, L. F. Sapucci, L. A. T. Machado, I. Vitorello, J. F. G. Monico, K. L. Holub, S. I. Gutman, N. Filizola, and R. A. Bennett, 2011: A dense GNSS meteorological network for observing deep convection in the Amazon. Atmosph. Sci. Lett., 12, 207–212, doi:10.1002/asl.312.

Adams, D. K., S. I. Gutman, K. L. Holub, and D. S. Pereira, 2013: GNSS Observations of Deep Convective Time scales in the Amazon, Geophys. Res. Lett., 40, doi:10.1002/grl.50573.

Adams D. K., R. Fernandes, K. Holub, S. Gutman, H. Barbosa, L. Machado, R. Bennett, R. Kursinski, L. Sapucci, C. DeMets, G. Chagas, A. Arellano, N. Filizola, A. Amorim, R. Araujo, L. Assunção, A. Calheiros, G. Cirino, T. Pauliquevis, B. Portela, A. Sa, J. Sousa, and L. Tanaka, 2015: The Amazon Dense GNSS Meteorological Network: A New Approach for Examining Water Vapor and Deep Convection Interactions in the Tropics. Bull. Amer. Meteor. Soc., doi: 10.1175/bams-d-13-00171.1.

Bastin, S., C. Champollion, O. Bock, P. Drobinski and F. Masson, 2005: On the use of GPS tomography to investigate water vapor variability during a Mistral/sea breeze event in southeastern France, Geophys. Res. Lett., 32, L05808, doi:10.1029/2004GL021907. Bennitt, G., and A. Jupp, 2012: Operational Assimilation of GPS Zenith Total Delay Observations into the Met Office Numerical Weather Prediction Models. Mon. Wea. Rev., 140, 2706–2719, doi:10.1175/MWR-D-11-00156.1.

Best, D.J., and D. E. Roberts, 1975: Algorithm AS 89: The Upper Tail Probabilities of Spearman's rho. J. Royal Statistical Society, 24, 377-379, doi: 10.2307/2347111.

Bevis, M. G., S. Susinger, T. Herring, C. Rocken, R. A. Anthes, and R. Ware, 1992: GPS Meteorology: Remote of Atmospheric Water Vapor Using the Global Positioning System. J. Geophys. Res., 97, D14, 15787-15801, doi: 10.1029/92JD01517.

Bevis, M., G. Chiswell, T. A. Herring, R. Anthes, C. Rocken, and E. R. H. Ware, 1994: GPS Meteorology: Mapping zenith wet delays into precipitable water. J. Appl. Meteor., 33, 379-386, doi:http://dx.doi.org/10.1175/1520-0450(1994)033<0379:GMMZWD>2.0.CO;2.

Bock, O., M. N. Bouin,E. Doerflinger, P. Collard, F. Masson, R. Meynadier, S. Nahmani, M. Koité, K. Gaptia Lawan Balawan, F. Didé, D. Ouedraogo, S. Pokperlaar, J.-B. Ngamini, J. P. Lafore, S. Janicot, F. Guichard, M. Nuret. 2008: The West African Monsoon observed with ground-based GPS receivers during AMMA, J. Geophys. Res., 113 (D21105) doi: 10.1029/2008JD010327.

Boehm, J., B. Werl, and H. Schuh, 2006: Troposphere mapping functions for GPS and VLBI from ECMWF operational analysis data. J. Geophys. Res., 111, B02406, doi:10.1029/2005JB003629.

Brenot, H., A. Walpersdorf, M. Reverdy, J. van Baelen, V. Ducrocq, C. Champollion, F. Masson, E. Doerflinger, E., Collard, P., and Giroux, P. 2014: A GPS network for tropospheric tomography in the framework of the Mediterranean hydrometeorological observatory C´evennes-Vivarais (southeastern France), Atmos. Meas. Tech., 7, 553-578, doi:10.5194/amt-7-553-2014.

Calheiros, A. J. P., and L. A. T. Machado, 2014: Cloud and rain liquid water statistics in the CHUVA campaign. Atmosph. Research, 144, 126-140, doi:http://dx.doi.org /10.1016/j.atmosres.2014.03.006.

Chan, P. W., 2009: Performance and application of a multi-wavelength, ground-based microwave radiometer in intense convective weather. Meteorol. Z., 18, 3, 253-265, doi:10.1127/0941-2948/2009/0375.

Cucurull, L., F. Vandenberghe, D. Barker, E. Vilaclara, and A. Rius, 2004: Three-Dimensional Variational Data Assimilation of Ground-Based GPS ZTD and Meteorological Observations during the 14 December 2001 Storm Event over the Western Mediterranean Sea. Mon. Wea. Rev., 132, 749–763, doi:http://dx.doi.org/10.1175/1520-0493(2004)132<0749:TVDAOG>2.0.CO;2.

Daubechies, I., 1992: Ten Lectures on Wavelets. Society for Industrial and Applied Mathematics, 357 pp.

Davis, J. L., T. A. Herring, I. Shapiro, A. E. Rogers, and G. Elgened, 1985: Geodesy by radio Interferometry: Effects of Atmospheric Modeling Errors on Estimates of BaseLine Length. Radio Sci., 20, 1593-1607, doi: 10.1029/RS020i006p01593.

Giangrande, S. E., T. Toto, A. Bansemer, M. R. Kumjian, S. Mishra, and A. V. Ryzhkov, 2016: Insights into riming and aggregation processes as revealed by aircraft, radar, and disdrometer observations for a 27 April 2011 widespread precipitation event, J. Geophys. Res. Atmos., 121, 5846–5863, doi:10.1002/2015JD024537.

Gematronik, 2007: Dual-polarization weather radar handbook. In: Bringi, V.N., Thurai, M., Hannesen, R. (Eds.), Selex-SI gematronik, 2nd edition (163 pp.).

Gregorius, T., 1996: GIPSY-OASIS II How it works. Department of Geomatics, University of Newcastle upon Tyne, 167 pp. [Available online at: http://web.gps.caltech.edu/classes/ge167/file/gipsy-oasisIIHowItWorks.pdf.].

Guerova G, J. Jones, J. Dousa, G. Dick, S. De Haan, E. Pottiaux, O. Bock, R. Pacione, G. Elgered, H. Vedel, M. Bender, 2016: Review of the state-of-the-art and future prospects of the ground-based GNSS meteorology in Europe. Atmos Meas Tech Discuss. doi:10.5194/amt-2016-125

de Haan, S. D., S. Barlag, H. K. Baltink, F. Debie, and H. V. Marel, 2004: Synergetic Use of GPS Water Vapor and Meteosat Images for Synoptic Weather Forecasting. J. Appl. Meteoro., 43, 514-518, doi:http://dx.doi.org/10.1175/1520-0450(2004)043<0514: SUOGWV>2.0.CO;2.

de Haan, S. D., 2006: Measuring Atmospheric Stability with GPS. J. Appl. Meteoro. Climatol., 45, 467-475, doi: http://dx.doi.org/10.1175/JAM2338.1.

de Haan, S. D., and I. Holleman, 2009: Real-Time Water Vapor Maps from a GPS Surface Network: Construction, Validation, and Applications. J. Appl. Meteoro. Climatol., 48, 1302-1316, doi: http://dx.doi.org/10.1175/2008JAMC2024.1.

Holloway, C. and J. Neelin, 2010: Temporal Relations of Column Water Vapor and Tropical Precipitation. J. Atmos. Sci., 67, 1091–1105, doi: http://dx.doi.org/10.1175/2009JAS3284.1.

Iwabuchi, T., C. Rocken, Z. Lukes, L. Mervat, J. Johnson, and M. Kanzaki, 2006: PPP and Network True Real-time 30 sec Estimation of ZTD in Dense and Giant Regional GPS Network and the Application of ZTD for Nowcasting of Heavy Rainfall. Proceedings of the 19th International Technical Meeting of the Satellite Division of The Institute of Navigation (ION GNS 2006), 1902-1909.

IERS Conventions, 2010: Gérard Petit and Brian Luzum (eds.). (IERS Technical Note ; 36) Frankfurt am Main: Verlag des Bundesamts für Kartographie und Geodäsie, 2010. 179 pp., ISBN 3-89888-989-6 https://www.iers.org/IERS/EN/Data Products/ Conventions/conventions.html.

Jerrett, D., and J. Nash, 2001: Potential Uses of Surface Based GPS Water Vapour Measurements for Meteorological Purposes. Phys. Chem. Earth (A), 26, 457-461, doi:10.1016/S1464-1895(01)00083-7.

Joss, J., and A. Waldvogel, 1967: Ein Spektrograph für Niederschlags-tropfen mit automatischer Auswertung (A spectrograph for rain drops with automatical analysis). Pure Appl. Geophys., 68, 240–246, http://dx.doi.org/10.1007/BF00874898.

Kinnell, P. I. A., 1976: Some Observations on the Joss-Waldvogel Rainfall Disdrometer, J. Appl. Meteor., 15, 499–502, doi:http://dx.doi.org/10.1175/1520-0450(1976)015<0499:SOOT JW>2.0.CO;2.

Kursinski, E. R., R. A. Bennett, D. Gochis, S. I. Gutman, K. L. Holub, R. Mastaler, C. Minjarez Sosa, I. Minjarez Sosa, and T. van Hove (2008), Water vapor and surface observations in northwestern Mexico during the 2004 NAME Enhanced Observing Period, Geophys. Res. Lett., 35, L03815, doi:10.1029/2007GL031404.

Lyard, F., F. Lefèvre, T. Letellier, and O. Francis, 2006: Modelling the global ocean tides: a modern insight from FES2004, Ocean Dynamics, 56, 394-415, doi:http://dx.doi.org/10.1007/s10236-006-0086-x.

Machado, L. A. T., M. A. F. Silva Dias, C. Morales, G. Fisch, D. Vila, R. Albrecht, S. J. Goodman, A. J. P. Calheiros, T. Biscaro, C. Kummerow, J. Cohen, D. Fitzjarrald, E. L. Nascimento, M. S. Sakamoto, C. Cunningham, J. P. Chaboureau, W. A. Petersen, D. K. Adams, L. Baldini, C. F. Angelis, L. F. Sapucci, P. Salio, H. M. J. Barbosa, E. Landulfo, R. A. F. Souza, R. J. Blakeslee, J. Bailey, S. Freitas, W. F. A. Lima, and A. Tokay, 2014: The Chuva Project: How Does Convection Vary across Brazil? Bull. Amer. Meteor. Soc., 95, 1365–1380, doi:http://dx.doi.org/10.1175/BAMS-D-13-00084.1.

Madhulatha, A., M. Rajeevan, M. Venkat Ratnam, J. Bhate, and C. V. Naidu, 2013: Nowcasting severe convective activity over southeast India using ground-based microwave radiometer observations. J. Geophys. Res., 118, doi:10.1029/2012JD018174.

Mazany, R. A., S. Businger, S. I. Gutman, and W. Roeder, 2002: A lightning prediction index that utilizes GPS integrated precipitable water vapor. Wea. Forecasting, 17, 1034–1047, doi:10.1175/1520-0434(2002)017<1034:ALPITU>2.0.CO;2.

Montenbruck, O., R. Schmid, F. Mercier, P. Steigenberger, C. Noll, R. Fatkulin, S. Kogure, A.S. Ganeshan, 2015: GNSS satellite geometry and attitude models, Advances in Space Research, 56, 6, 1015-1029. Doi:http://dx.doi.org/10.1016/j.asr.2015.06.019.

Moore, A., I. Small, S. Gutman, Y. Bock, J. Dumas, P. Fang, J. Haase, M. Jackson and J. Laber, 2015: National Weather Service Forecasters Use GPS Precipitable Water Vapor for Enhanced Situational Awareness during the Southern California Summer Monsoon. Bull. Amer. Meteor. Soc., 96, 1867–1877, doi: 10.1175/BAMS-D-14-00095.1. Muller, C. J., L. E. Back, P. A. O'Gorman, and K. A. Emanuel, 2009: A model for the relationship between tropical precipitation and column water vapor. Geophys. Res. Lett., 36, L16804, doi:10.1029/2009GL039667.

Percival, D. B., and A. T. Walden, 2000: Wavelet Methods for Time Series Analysis. Cambridge University, 594 pp.

Raymond, D. J. 1987: A Forced Gravity Wave Model of Serf-Organizing Convection. J. Atmo. Sci., 44, 23, 3528-3543.

Rocken, C., T. VanHove, M. Rothacher, F. Solheim, R. Ware, M. Bevis, S. Businger, and R. Chadwick, 1994: Towards near-real-time estimation of atmospheric water vapor with GPS. Eos Trans. AGU, 7544, Fall Meet. Suppl., 173.

Sapucci, L. F., 2014: Evaluation of Modeling Water-Vapor-Weighted Mean Tropospheric Temperature for GNSS-Integrated Water Vapor Estimates in Brazil. J. Appl. Meteor. Climatol., 53, 715–730, doi:http://dx.doi.org/10.1175/JAMC-D-13-048.1.

Sapucci, L. F., L. A. T. Machado, J. F. G. Monico, and A. Plana-Fattori, 2007: Intercomparison of Integrated Water Vapor Estimative from multi-sensor in Amazonian Regions. J. Atmos. Oceanic Technol., 24, 1880–1894, doi:http://dx.doi.org/10.1175/JTECH2090.1.

Serra, Yolande L., David K. Adams, Carlos Minjarez-Sosa, James M. Moker, Jr., Avelino Arellano, Christopher Castro, Arturo Quintanar, Luis Carlos Alatorre, Alfredo Granados-Olivas, Enrique Vazquez, Kirk L. Holub, Charles DeMets, 2016: The North American Monsoon GPS Transect Experiment 2013. *Bull. Amer. Meteor. Soc.*, **97**, 2103–2115, doi: 10.1175/BAMS-D-14-00250.1. Sato, T and F. Kimura, 2005: Diurnal Cycle of Convective Instability around the Central Mountains in Japan during the Warm Season. J. Atmo. Sci., 62, 1626-1636.

Schmid, R., P. Steigenberger, G. Gendt, M. Ge, M. Rothacher, 2007: Generation of a consistent absolute phase-center correction model for GPS receiver and satellite antennas. Journal of Geodesy, 81: 781. 81, 12, 781–798, doi:10.1007/s00190-007-0148-y

Shangguan, M., S. Heise, M. Bender, G. Dick, M. Ramatschi, and J. Wickert, 2015: Validation of GPS atmospheric water vapor with WVR data in satellite tracking mode, Ann. Geophys., 33, 55-61, doi:10.5194/angeo-33-55-2015.

Shi, J., X. Chaoqian, G. Jiming and G. Yang, 2015: Real-Time GPS precise point positioning-based precipitable water vapor estimation for rainfall monitoring and forecasting, IEEE Trans. Geosci. Remote Sens, vol.53, pp. 3452-3459, doi: 10.1109/TGRS.2014.2377041.

Comentário [s28]: Reviser1E16

Solheim, F. S., J. Vivekanandan, R. H. Ware, and C. Rocken, 1999: Propagation delays induced in GPS signals by dry air, water vapor, hydrometeors, and other particulates. J. Geophys. Res., 104, 9663–9670, doi:10.1029/1999JD900095.

Testud, J., E. L. Bouar, E. Obligis, and M. Ali-Mehenni, 2000: The Rain Profiling Algorithm Applied to Polarimetric Weather Radar. J. Atmos. Oceanic Technol., 17, 332–356, doi:http://dx.doi.org/10.1175/1520-0426(2000)017<0332:TRPAAT>2.0.CO;2.

Torrence, C., and G. P. Compo, 1998: A Practical Guide to Wavelet Analysis. Bull. Amer. Meteor. Soc., 79, 61-78.

Whitcher, P., D. B. Guttorp, and B. Percival, 2000: Wavelet analysis of covariance with application to atmospheric time series. J. Geophys. Res., 105, 14941–14962, doi::10.1029/2000JD900110.

Wolfe, D. E., and S. I. Gutman, 2000: Developing an operational, surface-based, GPS, water vapor observing system for NOAA: Network Design and Results. J. Atmos. Ocean. Technol., 17, 426-440.

Zumberge, J. F., M. B. Heflin, D. C. Jefferson, M. M. Watkins, and F. H. Webb (1997), Precise point positioning for the efficient and robust analysis of GPS data from large networks, J. Geophys. Res., 102(B3), 5005–5017, doi:10.1029/96JB03860.

Tables

Table 1: Configuration items associated with ZTD estimates and respective values used GPS data processing using GOA-II software.

Configuration item	Parameter used	Comments
GPS data file for GOA-II	Rinex format in sampling rate of 1 second	Data collection from CHUVA
Mapping function	Global Mapping Function (Boehm et al. 2006)	Selected in the data processing
Cut-off elevation angle:	10°	Selected in the data processing
Elevation weight in the Mapping function	Elevation dependent and apply 3 coefficients depend on the latitude and height above sea level of the observing site and on the DoY	(Boehm et al. 2006)
ZHD a priori	Constant using a Tropospheric model in function of high of the GPS station (2.126 m)	Default values
ZWD a priori	Constant (0.10 m)	Default values
Process noise for tropospheric delay	Random walk	Default values
Maximum drift for tropospheric delay	8.333E-8 (km per square-root second);	Default values
Tropospheric Gradients estimates	yes	Default values
Maximum drift for Gradients estimates	8.333E-9 (km per square-root second)	Default values
Sampling rate of the ZTD estimates	60 seconds	Selected in the data processing

Table 2: Precipitation events observed by radar during CHUVA Vale experiment in different extension terciles as a function of the precipitation fractions above 35 mm h^{-1}.

Event	DoY	Maximal radar precipitation UTC Time (hh:mm)	Precipitation fraction observed by XPol radar (%)			Terciles
			Above 50 mm h^{-1}	Above 35 mm h^{-1}	Above 20 mm h^{-1}	
1	348	02:42	73	85	95	
2	354	21:12	28	45	63	
3	341	18:36	36	41	45	Upper
4	315	17:12	26	41	49	tercile
5	335	19:24	30	38	42	
6	352	20:00	2	33	84	
7	342	16:36	24	27	28	
8	326	21:18	8	26	45	
9	343	01:06	4	9	15	Middle
10	338	20:18	0	8	19	tercile
11	332	19:18	5	5	5	
12	333	19:42	0	2	8	
13	314	21:06	2	2	7	
14	327	00:36	0	1	25	
15	358	23:00	0	1	10	Lower
16	317	21:48	0	1	2	tercile
17	318	08:48	0	0	19	
18	331	17:12	0	0	2	

Table 3. Statistical measurements of the GPS-PWV derivative for different extension terciles of precipitation events.

Statistical Measurements	Other cases	Terciles		
		Lower	Middle	Upper
Average value (mm h^{-1})	+0.04	-0.18	-0.38	0.13
Standard deviation (mm h^{-1})	±2.52	±3.18	±4.76	±5.57
Median (mm h^{-1})	0.00	0.00	+0.29	+0.65
Mode (mm h^{-1})	0.00	0.00	+1.00	+1.00
Maximal value (mm h^{-1})	+21.13	+8.42	+11.00	+13.25
Minimal value (mm h^{-1})	-19.07	-6.99	-17.30	-14.15
% > +9.5 mm h^{-1}	0.21%	0.00%	0.78%	7.81%
% < -9.5 mm h^{-1}	0.38%	0.00%	4.68%	5.47%

Figures

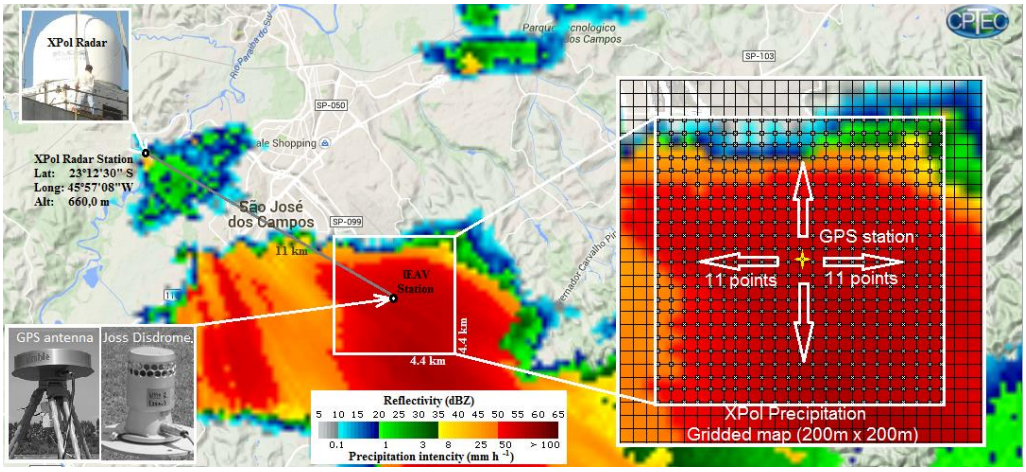

Figure 1: Illustration of the CHUVA Vale experiment, in which the sites where the XPol radar, GPS receiver and disdrometer were installed are indicated. The area of 4.4 km per 4.4 km around the GPS station is highlighted in this figure over the precipitation field observed by XPol radar on December 14th (DoY 348) of 2011. Some details about the composition of this area using the points of the XPol gridded map are additionally presented.

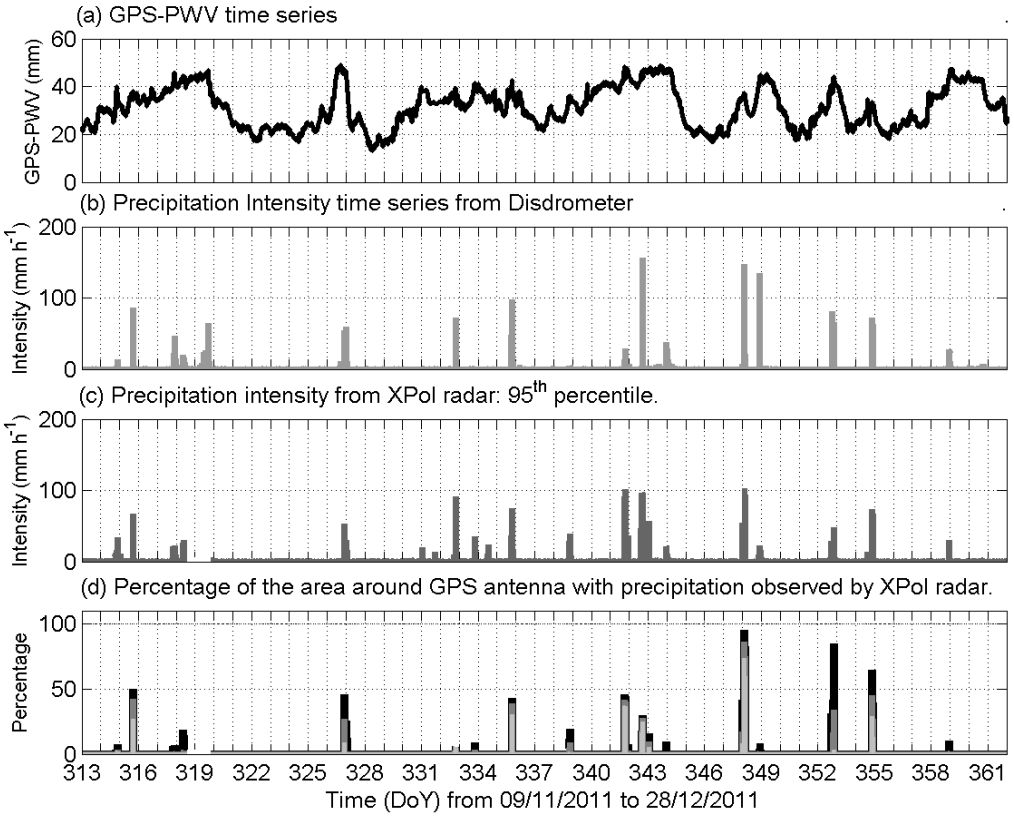

Figure 2: Time series of the precipitation and GPS-PWV obtained during CHUVA Vale campaign: (a) GPS-PWV time series; (b) precipitation intensity observed by Joss disdrometer; (c) 95th percentile of the precipitation intensity observed by XPol radar in the area of 4.4 km per 4.4 km centered on the GPS antenna; and (d) precipitation fraction in the area of 4.4 km per 4.4 km centered on the GPS antenna, where the black bar is the fraction above 20 mm h^{-1}, the dark gray bar is the fraction above 35 mm h^{-1} and the light gray bar is the fraction above 50 mm h^{-1}.

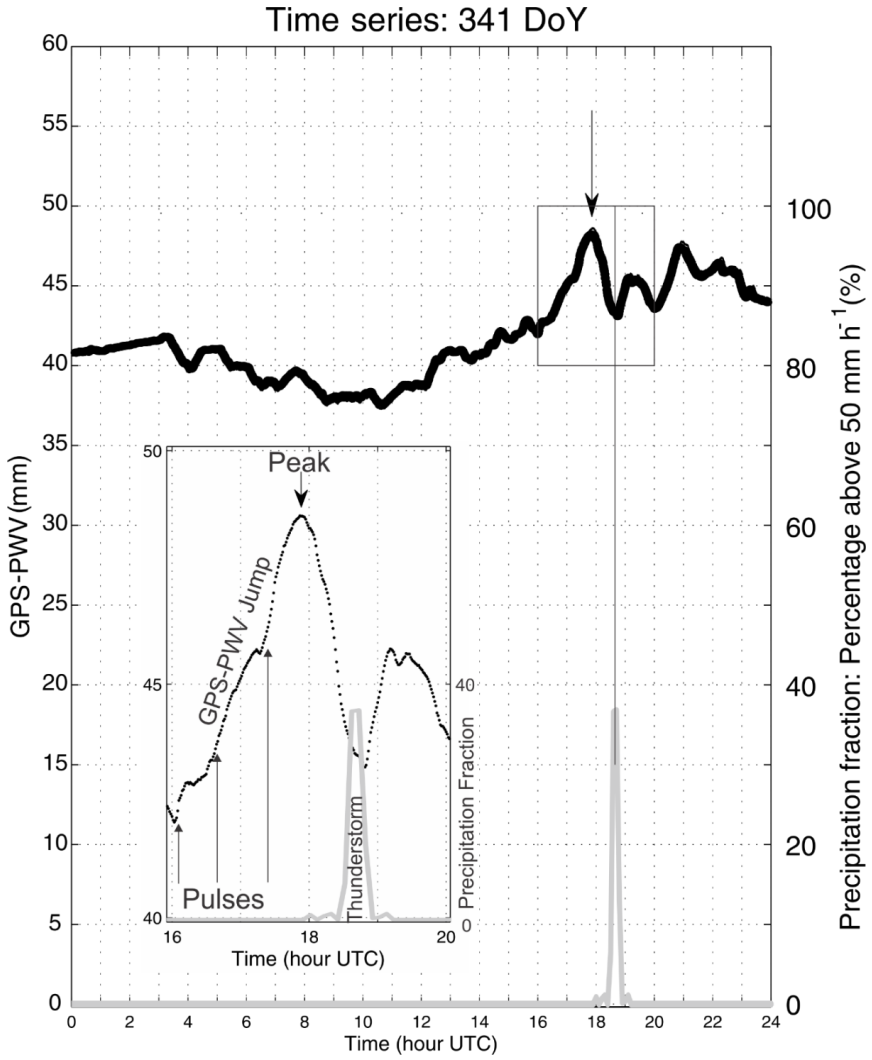

Figure 3: GPS-PWV jump observed in the 2-hour period before a heavy storm occurred during DoY 341 (1836 UTC 7 December 2011).

Comentário [s29]: Reviser1E15

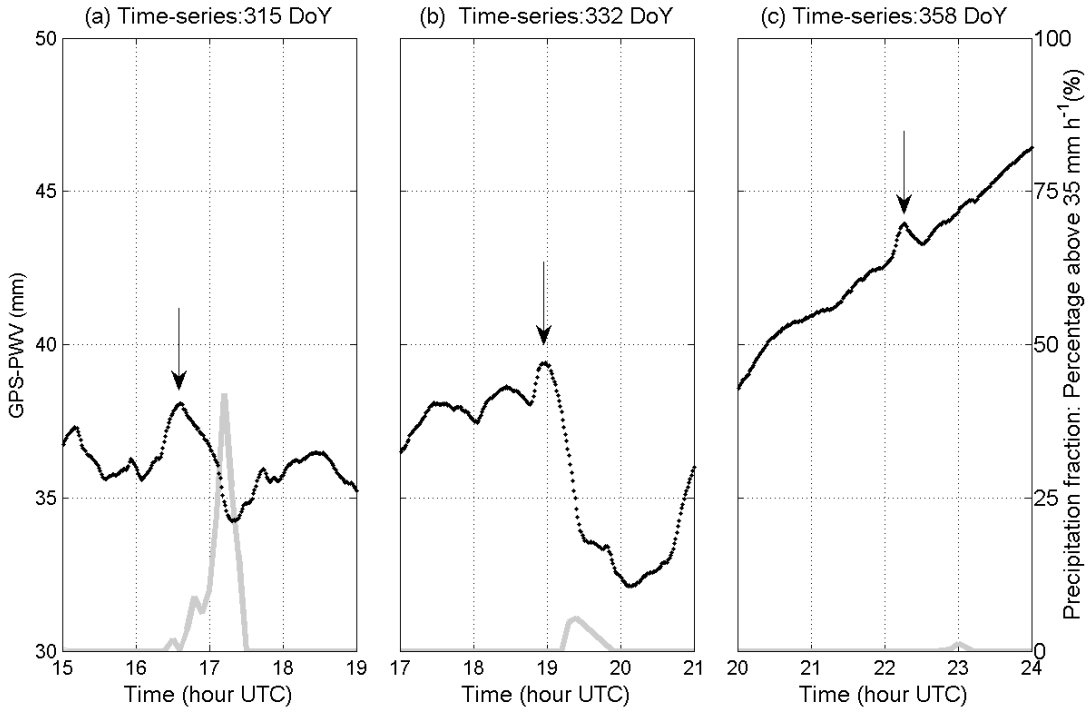

Figure 4: Other cases of GPS-PWV jumps observed before precipitation events with fraction above 35 mm h^{-1} of different extension occurred during (a) DoY 315 (1712 UTC), (b) DoY 332 (1918 UTC) and (c) DoY 358 (2300 UTC).

Comentário [s30]: Reviser1E17

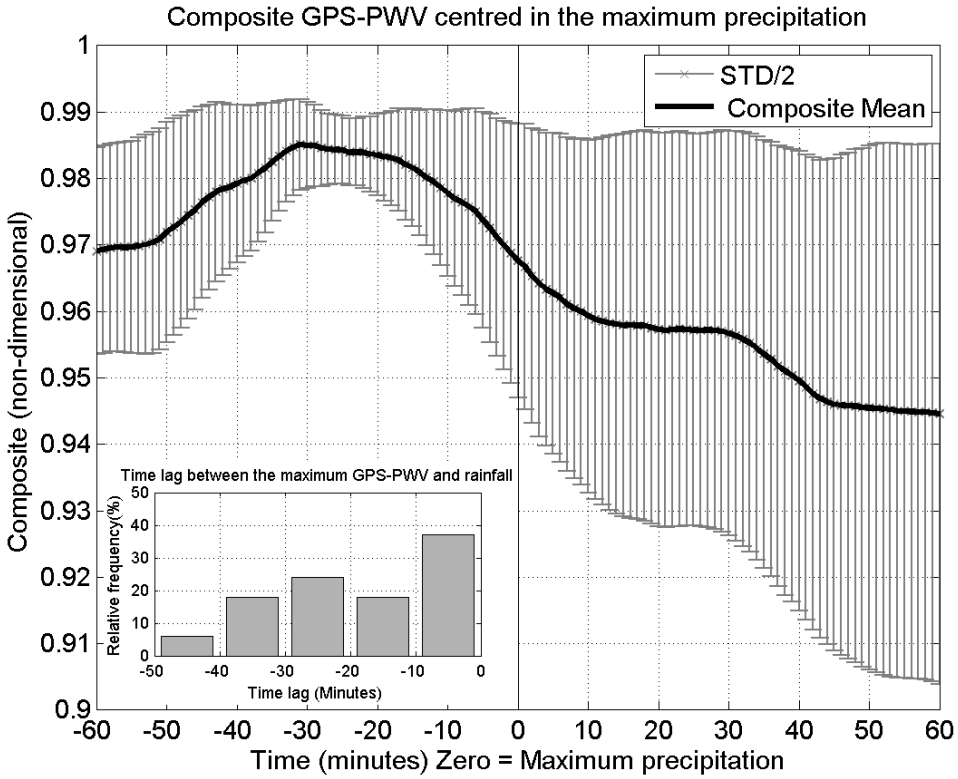

Figure 5: Composite the GPS-PWV time series 60 minutes before and 60 minutes after of 18 precipitation events listed by Table 2 and the distribution of the time lag between the maximum GPS-PWV and the time of the maximum rainfall of these events (precipitation fraction above 35 mm h^{-1} in the area of 4.4 km per 4.4 km centered on the GPS).

Comentário [s31]: Reviser1E17

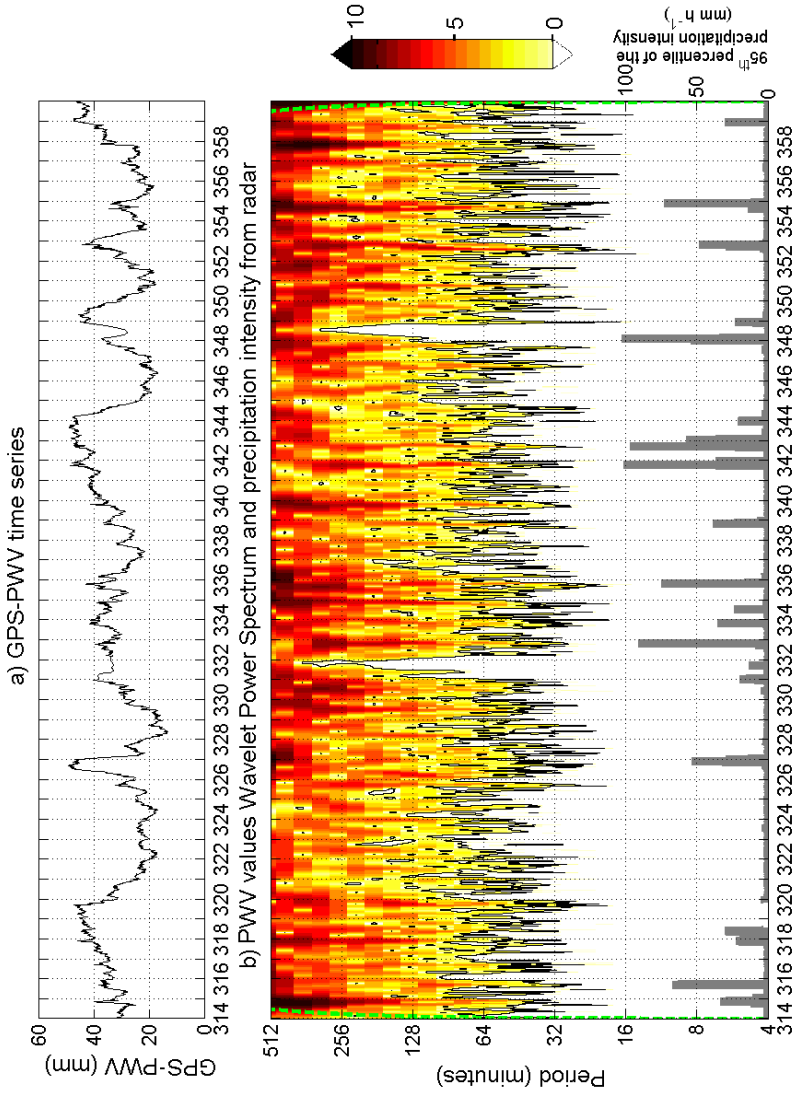

Figure 6: GPS-PWV time series at IEAV station (a) and wavelet power spectrum analysis (b). The cone of influence is plotted in green dashed line to avoid interpretations in border regions. The precipitation intensity values observed by XPol radar (95th percentile) in the area of 4.4 km per 4.4 km around the GPS antenna are included in the bottom of this plot.

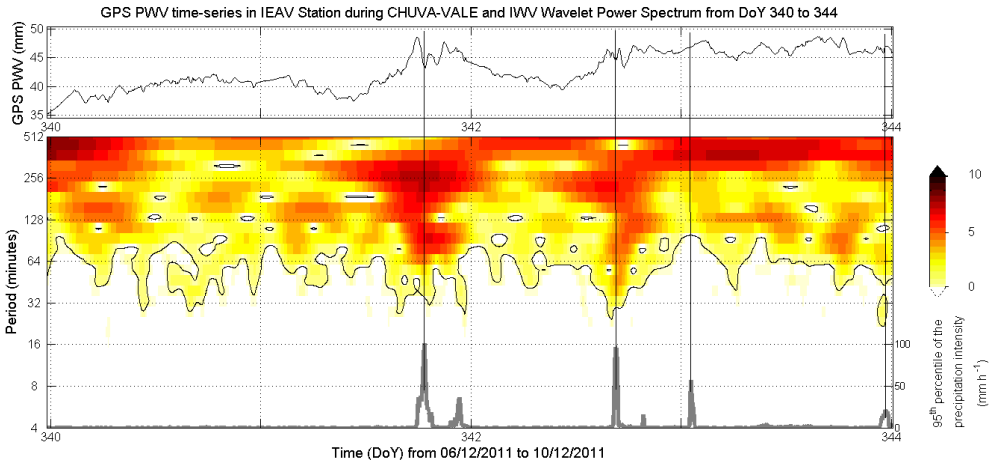

Figure 7: Similar to Fig. 6 for a shorter period (from 0000 UTC on DoY 340 to 0000 UTC on DoY 344) to emphasize the details in the wavelet power spectrum during the occurrence of precipitation events. This period is inside of the cone of influence. A vertical line was drawn for each precipitation maximum to make easier the analysis.

Comentário [s32]: Reviser1E12

5

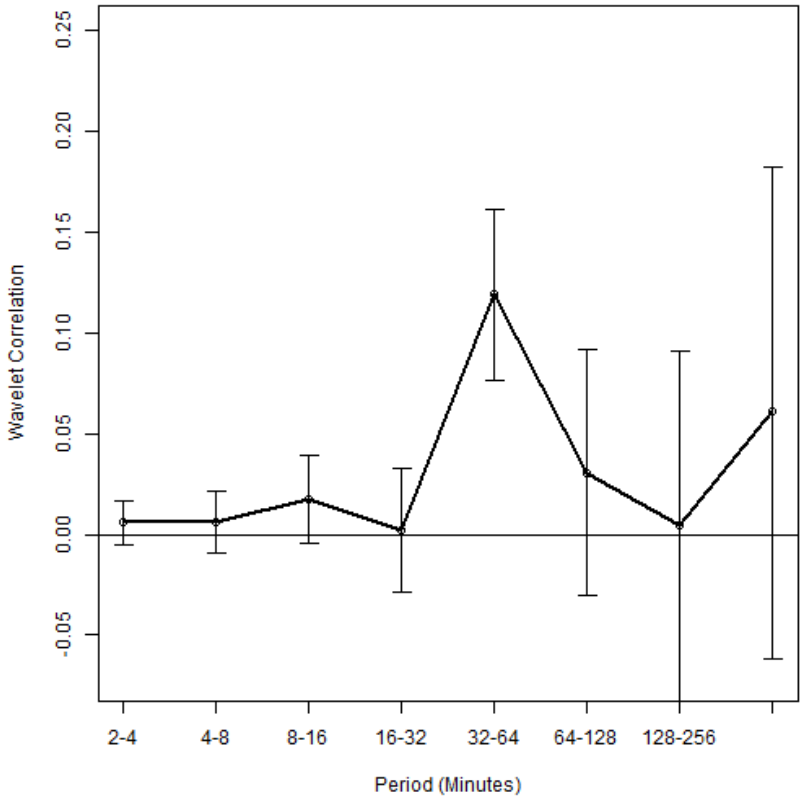

Figure 8: Wavelet correlation values between GPS-PWV and 95th percentile of the precipitation intensity from XPol radar time series as a function of the different wavelet scales represented by their respective time periods. The correlation is estimated considering the lag zero.. The 95% Confidence Interval for each WCC is estimated considering a Gaussian Distribution after applying the Fisher`s Z Transformation (Whitcher et al. 2000).

Comentário [s33]: Reviser1E14

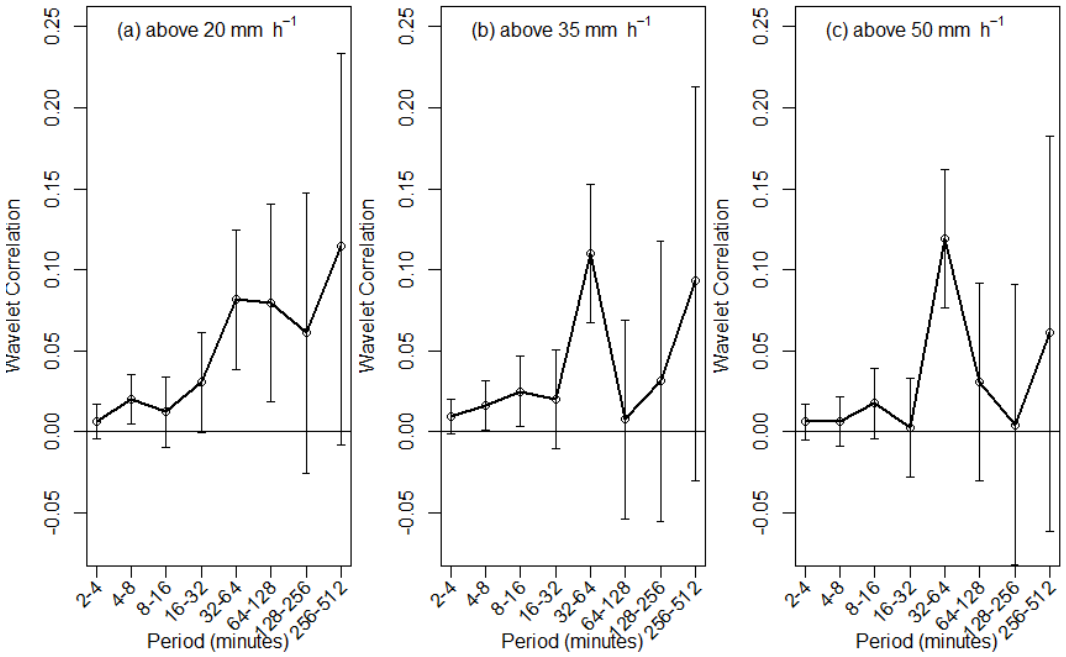

Figure 9: Wavelet correlation values between GPS-PWV and precipitation time series in different wavelet scales (represented by their respective time periods) for (a) percentage of points above 20 mm h^{-1} observed by radar around the GPS antenna; (b) the same above 35 mm h^{-1}; (c) and the same above 50 mm h-1. The correlation is estimated considering the lag zero. The 95% Confidence Interval for each WCC is estimated considering a Gaussian Distribution after applying the Fisher`s Z Transformation (Whitcher et al. 2000).

Comentário [s34]: Reviser1E14

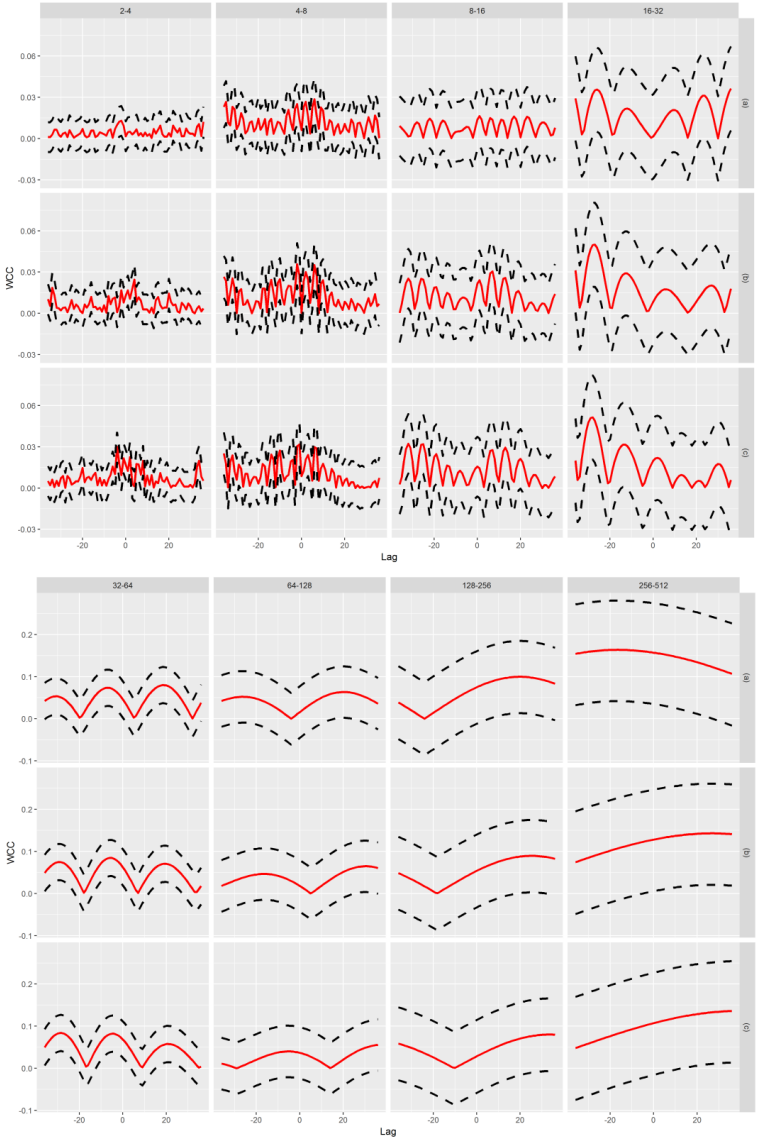

Figure 10: Wavelet cross-correlation values between GPS-PWV and (a) percentage of points above 20 mm h^{-1} observed by radar around the GPS antenna; (b) the same above 35 mm h^{-1}; (c) and the same above 50 mm h-1; as function of lead-lag for different time periods. The dotted line represents the 95% confidence interval.

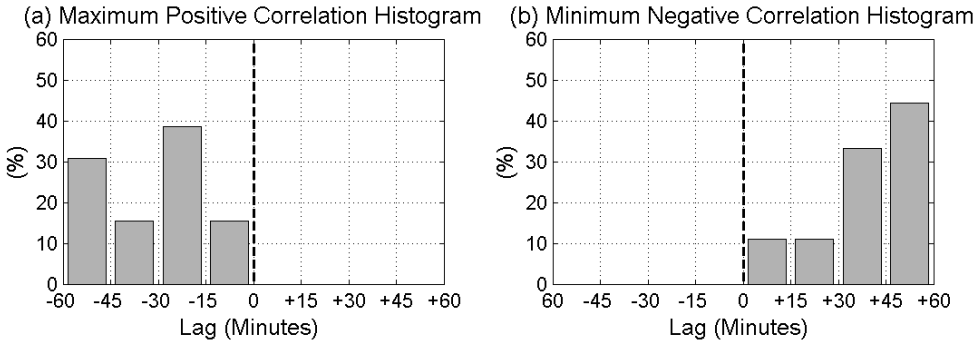

Figure 11: Spearman correlation histograms of maximum positive (a) and minimum negative (b) correlations as functions of the lag of occurrence for GPS-PWV values and precipitation events. All 18 precipitation events listed in Table 2 were taken into account in this analysis.

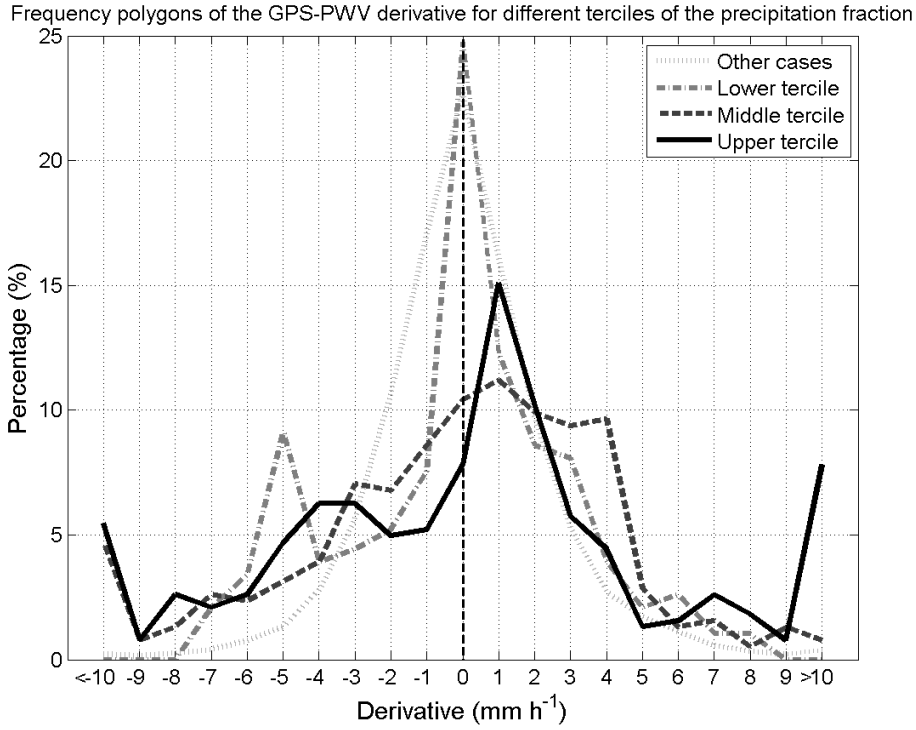

Figure 12: Frequency polygons of the GPS-PWV derivatives calculated over the period of 60 minutes before precipitation events for different terciles of the precipitation fraction above 35 mm h^{-1} observed using XPol radar.

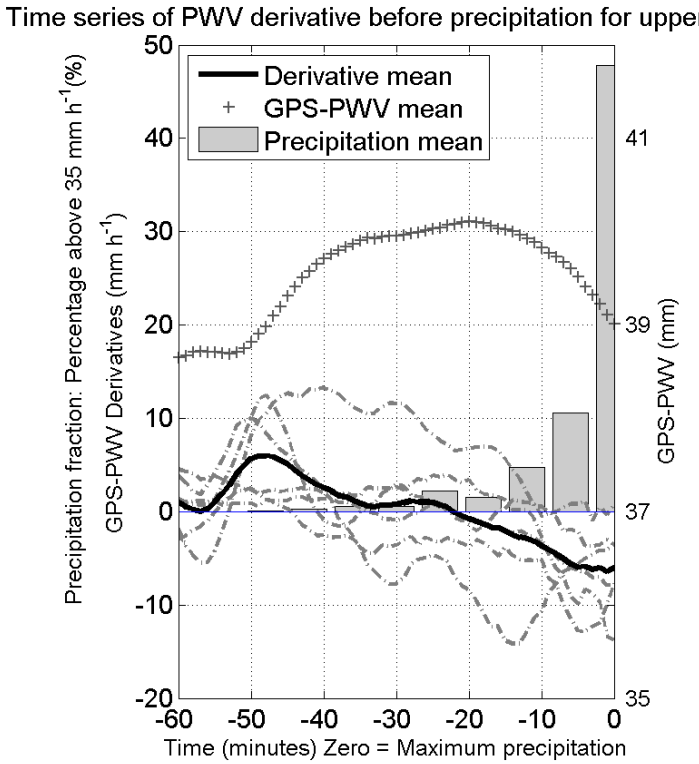

Figure 13: Time series of GPS-PWV derivative before precipitation for upper terciles. The mean values of GPS-PWV derivative, precipitation and GPS-PWV for this events are also shown in this figure.

5